Astron. Astrophys. 353, 624–640 (2000)

ASTRONOMY AND ASTROPHYSICS

A 0.4–20 μm spectroscopic study of the clumped wind of WR 147*

P.W. Morris[1,2], **K.A. van der Hucht**[2], **P.A. Crowther**[3], **D.J. Hillier**[4], **L. Dessart**[3], **P.M. Williams**[5], **and A.J. Willis**[3]

[1] Astronomical Institute "Anton Pannekoek", University of Amsterdam, 1098 SJ Amsterdam, The Netherlands
[2] Space Research Organization Netherlands, Sorbonnelaan 2, 3584 CA Utrecht, The Netherlands
[3] Department of Physics and Astronomy, University College London, Gower St., London, UK
[4] Department of Physics and Astronomy, University of Pittsburgh, Pittsburgh, PA 15260, USA
[5] Institute for Astronomy, University of Edinburgh, Royal Observatory, Edinburgh EH9 3HJ, UK

Received 22 July 1999 / Accepted 22 October 1999

Abstract. We present a detailed spectroscopic study of the WN8(h)+B0.5 V binary system WR 147 using a non-LTE model that incorporates advances in line blanketing and allows for clumping in the wind. Ground-based optical and near-infrared observations, and high-resolution spectra obtained with the *ISO Short Wavelength Spectrometer* are combined for this study. Previously derived interstellar extinction values of $E_{B-V} \simeq 4.1$ mag at $R_V \simeq 2.7$ are confirmed here. The distance to WR 147 is revised slightly upwards to 650 pc, based on Galactic and LMC WN8–9 calibrators in the K band. An infrared extinction curve for this sightline reveals absorption bands at 9.7 and 18 μm that are stronger than expected for the average ISM, but the nature and location of the intervening material is unknown.

He line profiles of the WN8 star exhibit clear evidence for clumping in the wind. We find that a volume filling factor f of 0.1 yields line profiles which match observations (emphasizing the electron scattering wings), though values of f in the range of 0.04 to 0.25 are reasonable. This leads to a mass-loss rate range of (1.5–3.7)$\times 10^{-5}$ M$_\odot$ yr^{-1}, substantially lower than derived from optical or radio observations under assumptions of homogeneity. Additionally including the effects of line-blanketing, the wind performance factor, $\dot{M}v_\infty/(L_*/c)$, is reduced to $\sim$2.5.

Hydrogen is severely depleted, but present at 9% by mass. Observations of the [Ca IV] 3.21 μm, [S IV] 10.51 μm, and [Ne III] 15.56 μm fine structure lines, from which we measure a terminal wind velocity of $\sim$950 km s^{-1}, allow us to place constraints on the surface abundances of these elements. In all cases we find good agreement with cosmic abundances (adjusted to a hydrogen-poor environment) and thus with evolutionary predictions for WN stars.

Key words: stars: abundances – stars: fundamental parameters – stars: Wolf-Rayet – infrared: stars

1. Introduction

WN8 stars are reputed to be the most active subclass of Wolf-Rayet (WR) stars because of their high levels of spectroscopic and photometric variability (Lamontagne & Moffat 1987; Moffat et al. 1989; Robert et al. 1989; Marchenko et al. 1994, 1998; Antokhin et al. 1995). Visual lightcurve amplitudes of 0.05−0.1 mag are intermediate between those of OIII-I stars and the microvariational amplitudes of Luminous Blue Variables (LBVs), according to Marchenko et al. (1998; see also Moffat et al. 1989), and may be accompanied by variations in the absorption components of optical P-Cygni lines (Marchenko et al. 1998), or by narrow emission subpeaks which propagate outwards from emission line center (Lépine & Moffat 1999). These typically occur on timescales of days. Besides the high variability, other phenomenological similarities exist between some WN8 stars and LBVs, such as ejected nebulae, low binary frequency, and spatial distribution, leading Crowther et al. (1995a) to suggest that WN8 stars may be immediately descended from LBVs, at least in some cases. This is plausible according to models of massive star evolution (Langer et al. 1994; Maeder 1996).

The stochastic line profile variations have been interpreted to be associated with inhomogeneities propagating outward in the rapidly expanding envelopes surrounding the stellar cores (e.g., Moffat 1996, 1999). It is believed that *all* hot star winds show stochastic line profile variations, indicating some hierarchy of wind clumping. If clumping affects the structure of a WR wind, and observations indicate that it does (e.g., Marchenko et al. 1998), then it should lead to a revision of the stellar and wind parameters spectroscopically derived using "standard" model assumptions, namely, that the outflows are spherical and homogeneous (Hillier 1991, 1995; Moffat & Robert 1994; Hamann & Koesterke 1998a; Nugis et al. 1998). The derived value of the mass-loss rate $\dot{M}$ is especially sensitive to these assumptions. According to the way in which clumping is parameterized in the latest non-LTE wind models (cf. Hillier & Miller 1999), the wind is uniformly clumped with a volume filling factor f, and

Send offprint requests to: P.W. Morris (pmorris@astro.uva.nl)

* Based on observations made with: *ISO*, a project of ESA with the participation of ISAS and NASA; the *ISO-SWS*, a joint project of SRON and MPE with contributions from KU-Leuven, Steward Observatory, and Phillips Laboratory; the Isaac Newton Telescope, which is operated on the island of La Palma by the Isaac Newton Group in the Spanish Observatorio del Roque de los Muchados of the Instituto de Astrofisica de Canarias; and the United Kingdom Infrared Telescope (UKIRT), operated on Mauna Kea, Hawaii, by the Joint Astronomy Centre and Royal Observatory Edinburgh.

empty between the clumps. The filling factor depends on the shape of the wind velocity curve $v(r)$, and $\dot{M}/\sqrt{f}$ becomes a fitting parameter. The wind is homogeneous when $f = 1$, and the mass-loss rate is lowered in models where $f < 1$. While this formulation may be simplistic in its representation of real Wolf-Rayet winds, Hillier & Miller (1999) have stressed in application to the WC5 star WR111 that it succeeds in generating line profiles with weaker electron scattering wings, more consistent with observations. Hamann & Koesterke (1998a) have found reasonably good fits to the emission line profiles in spectra of three WN stars using a filling factor of 1/4. This decreases the mass-loss rates derived from homogeneous wind models by a factor of two overall.

The impact of clumping in the spectroscopic analyses of WR winds should be clearly evident with the WN8 stars, if their spectroscopic activity is indeed a manifestation of wind inhomogeneities. The second closest WR star, WR 147 (AS 431), is a very long-period ($\sim 10^3$ years) binary, with WN8 and OB-type components. Williams et al. (1997; hereafter W97) have resolved clumps in the wind of the WN8 star on a scale of $\sim$20 mas using MERLIN, so the spectrum of this star seems ideal for study using the latest non-LTE, line-blanketed wind models that incorporate clumping into the description of the wind structure. Despite its close proximity of $\sim$0.6 kpc, however, WR 147 has been very difficult to observe because of unusually high extinction by dust, $A_V \simeq 12$ mag based on the near-infrared colors of the WN8 star (Churchwell et al. 1992; hereafter C92). In the C92 study, the high angular resolution observations with the VLA confirmed the presence of the companion, approximately 0.6″ to the north (thus referred to as WR 147N) of the optical position of the WN8 star (WR 147S), previously resolved by MERLIN (Moran et al. 1989). IR images by W97 set the projected separation at 0.64″, or at least 400 AU at a distance of 0.63 kpc. WR 147N is a source of non-thermal radio emission, interpreted as colliding wind effects (C92; W97; Contreras & Rodríguez 1999), and is classified as B0.5 V by W97, consistent with the ratio of visual brightnesses of the two sources measured with HST–WFPC2 (Niemela et al. 1998). WR 147S is the thermal main component, and is reported to have varied in 3.6 cm flux by $\sim$25% between 1995 and 1996 (Contreras & Rodríguez 1999). Variability of WR 147S at 6 cm has been reported by Watson et al. (1999). The 3.6 cm VLA observations by Contreras & Rodríguez (1999) also confirm the presence of inhomogeneities in the outflow of WR 147S, which appears spherically symmetric in their contour maps. Combined variations of WR147 (N+S) have been reported by van der Hucht et al. (1995) and by Skinner et al. (1999).

Prior to this study, the stellar and wind parameters of WR 147S were estimated by C92, using VLA measurements of the free-free radio continuum (see also Nugis et al. 1998), and by Hamann et al. (1995) and Hamann & Koesterke (1998b) using a standard model analysis of the optical spectrum. In this paper we present a new spectroscopic analysis of WR 147, using 2.4−20 μm spectra obtained with the *Short Wavelength Spectrometer* (*SWS*) onboard the *Infrared Space Observatory* (*ISO*), ground-based H and K band spectra obtained at the United Kingdom InfraRed Telescope (UKIRT), and optical spectra from the Isaac Newton Telescope (INT). This is the first detailed study of a WN-type WR star to incorporate mid-infrared spectroscopy.

A preliminary description of the *SWS* observations was given by van der Hucht et al. (1996), who estimated the terminal velocity of the WN8 wind to be 965 ± 20 km s^{-1} from the outer wind fine structure lines. Morris et al. (1998) later estimated the Ne/He abundance ratio from the observed [Ne III] 15.55μm line flux and the assumption of H/He = 0 based on a recombination analysis over the *SWS* wavelength range, and found evidence for a Ne/He enhancement by a factor of 2–3. This is in apparent conflict with evolutionary predictions for abundances at the surfaces of WR stars (cf. Maeder 1991; Meynet 1999). To make this determination, however, Morris et al. relied on standard model results by Hamann & Koesterke (1998b) for the value of $\dot{M}$, rescaled to the reddening and distance values given by C92. It was further realized by Morris et al. (1998) that the ionic abundance estimates are very sensitive to the value of $\dot{M}$, which is in general an uncertain quantity for WR stars due to distance and reddening uncertainties. In view of the unexpected Ne/He value, its sensitivity to the value of $\dot{M}$, and the evidence for clumping in the wind of WR 147S, we are highly motivated to seek new solutions for the star's physical properties using the widest available range of spectroscopy and the latest non-LTE, line-blanketed wind models in which the assumption of homogeneity can be relaxed. The results will be demonstrative of the impact of wind clumping in spectroscopic analyses for the purpose of determining chemical abundances and the mass-loss rates on which they rely.

The remainder of this paper is organized as follows. The observations are described in Sect. 2. The wind models and results of the spectroscopic analyses are presented in Sect. 3. In Sect. 3.2 we discuss the method for estimating ionic abundances of neon, sulphur, and calcium, and summarize the results of this study in Sect. 4. An extensive list of transitions deemed as likely contributors to the line emission over the *SWS* wavelengths is provided in the Appendix.

2. Observations

We present previously unpublished optical and IR spectroscopy of WR 147, obtained at the Isaac Newton Telescope (INT), La Palma, and with the *Infrared Space Observatory*, respectively.

2.1. ISO spectroscopy

WR 147 was observed twice with the *ISO-SWS* (de Graauw et al. 1996) grating sections in different instrument observing modes. The first observation was obtained on 4 January 1996 using *SWS* Astronomical Observing Template number 6, or AOT6, yielding spectral resolutions and signal-to-noise (S/N) ratios superior to the second observation, obtained 290 days later using *SWS* AOT1 at speed 3. Only the AOT6 observation is used in the spectroscopic analyses, but both observations were coadded in order to improve the S/N in the continuum near the 10 μm silicate absorption feature (discussed below). Both observations

were compared for photometric and line profile variability, but no meaningful variations were revealed. The line identifications given in the Appendix also make use of both observations.

The AOT6 was obtained during the *ISO* performance verification (PV) phase of the spacecraft systems and scientific instruments. The 2.4–29.5μm range was covered with several individual scans performed "up" and "down" with grating position to give continuum S/N ratios greater than 50 at $\lambda \leq 19$ μm, and 10–50 at the longer wavelengths. Based on signal estimates from K-band spectrophotometry and *IRAS* 12 and 25 μm PSC fluxes, the number of scans was two, four, or six, depending on sensitivities at key wavelengths within each "AOT band"[1]. Each scan was individually processed using software and calibration files compatible with ESA's version 6.0 or later of the *ISO* data product pipeline, producing calibrated spectral segments on a detector and scan basis. Each segment was then inspected for discontinuous dark current behaviour, and initially removed where jumps were noticed. The mean flux level within each resolution bin was defined using the stable detector output. The less stable output was then re-incorporated by fitting the regions between the jumps with a first or second order polynomial, and rectifying the output to the mean flux. This method results in improvements of 10–25% in continuum S/N ratios. The data were then cleaned for outlying points, and coadded to the *SWS*-AOT6 spectral resolution, which is $\lambda/\Delta\lambda \simeq 1400$–$3000$.

Absolute flux calibration uncertainties are generally 5–30% for observations obtained during the PV phase, given by the spread of photometric responsivities to celestial calibrators. The scatter is chiefly a result of spacecraft random pointing errors during this time (typically $\sim$4″) and the spatial responsivities of *SWS*. For a science observation that is also mispointed, discontinuities in flux between the different AOT bands can be noticed. The flux continuity in the WR 147 observation was extremely good, indicating nominal pointing. Furthermore, IRAS PSC flux at 25 μm is in agreement with the *SWS* mean 24–26 μm flux to within 4%. The IRAS PSC flux at 12 μm, however, overestimates the continuum by $\simeq$35% due to the strong HeI+H 12.37μm emission line. We estimate the flux calibration uncertainties to be: 5% in *SWS* band 1 (2.38–4.10 μm); 12% in band 2 (4.10–12.0 μm); and 20% in band 3 (12.0–27.6 μm). Recently, Smith & Houck (1999) presented ground-based 8$-$13 μm spectrophotometry of WR 147 obtained with the Cornelle Echelle Spectrograph, in excellent agreement with the *SWS* data over this wavelength range.

2.2. Optical and near-IR spectroscopy

Low resolution blue-yellow spectrophotometry of WR 147 was obtained at Kitt Peak National Observatory (KPNO) during observing runs in the 1980–1983 period (Massey 1984), later supplemented at KPNO by red and far-red spectrophotometry during 1989 (Conti et al. 1990). Synthetic filter photometry in the system of Smith (1968) gives v = 14.89 mag (Massey 1984). Niemela et al. (1998) acquired photometry of WR 147 using HST–WFPC2, revealing $V_{\rm WN8}$ = 13.86 mag and $V_{\rm B0.5\,V}$ = 16.02 mag, which precisely corresponds to the KPNO spectrophotometry for the combined system ($V_{\rm WR\,147}$=13.72 mag) given by convolution of the V band filter with the optical continuum with its steep rise towards longer wavelengths.

A substantially higher resolution optical spectrum of WR 147 was obtained at the INT on 22 July 1996, using the Intermediate Dispersion Spectrograph with the 235mm camera, and a 1024$\times$1024 Tektronix CCD. Complete spectral coverage over the 3700$-$6800 Å range was obtained at a two-pixel spectral resolution of 1.5 Å using a 1.5″ slit plus 1200 lines/mm gratings at four overlapping settings. A standard data reduction within IRAF (V2.10) was carried out, including subtraction of bias voltages, response flat-fielding, sky subtraction and object extraction. The wavelength scale was calibrated using CuAr or CuNe exposures, taken either before or after every stellar frame. Relative flux calibration was obtained by observing BD+28° 4211 (Oke 1990) at a similar airmass, although since these data were obtained through a narrow-slit, absolute spectrophotometry was not achieved.

We also make use of the 2-μm spectrum of WR 147 observed with the CGS2 spectrometer on the United Kingdom Infrared Telescope (UKIRT) in the UKIRT Service Observing Programme on 23 June 1990. A portion of this spectrum was published and used by C92 for determination of the terminal wind velocity of WR 147. Flux calibration and correction for the strong atmospheric CO_2 absorption features were provided by observation of the F8 supergiant BS 7796 at the same airmass as the observation of WR 147. The resolution of the spectra, determined by the size of the detectors, was $R \simeq 600$.

2.3. The remarkable interstellar extinction towards WR 147

Using the combined optical+IR spectral energy distribution, we have re-examined the interstellar extinction properties of the WR 147 sightline by comparing the de-reddened distribution to the theoretical models discussed below. The presence of the companion having the K-band luminosity of a B0.5 V star (cf. W97) has been accounted for by including a Kurucz $T_{\rm eff}$ = 29000 K, log(g) = 4 spectral energy distribution, following the B star temperature calibration of Crowther (1997), appropriately weighted relative to the WNL flux distribution (following Niemela et al. 1998).

We adopted the ultraviolet to near-IR extinction law of Cardelli et al. (1989), which is tabulated to 3.6 μm over a range of R_V ($\equiv A_V/E_{B-V}$). Other laws fixed to standard values of R_V of 3.1 or 3.2, namely Howarth (1983) and Steenman & Thé (1989), give reasonably good agreement over most wavelengths. For $\lambda > 3.6$ μm we have adopted the mid-IR extinction curve kindly provided by Dr. M. Cohen (priv. comm.), which accounts for the presence of interstellar silicate absorption bands at 9.7 and 18 μm. This curve generally agrees quite well with that of Rieke & Lebofsky (1985), as described by Cohen (1993). Dur-

[1] The *SWS* AOT bands specify the wavelength regime where photometric response is highest for each detector material used with different aperture and order-separating filter combinations. See de Graauw et al. (1996).

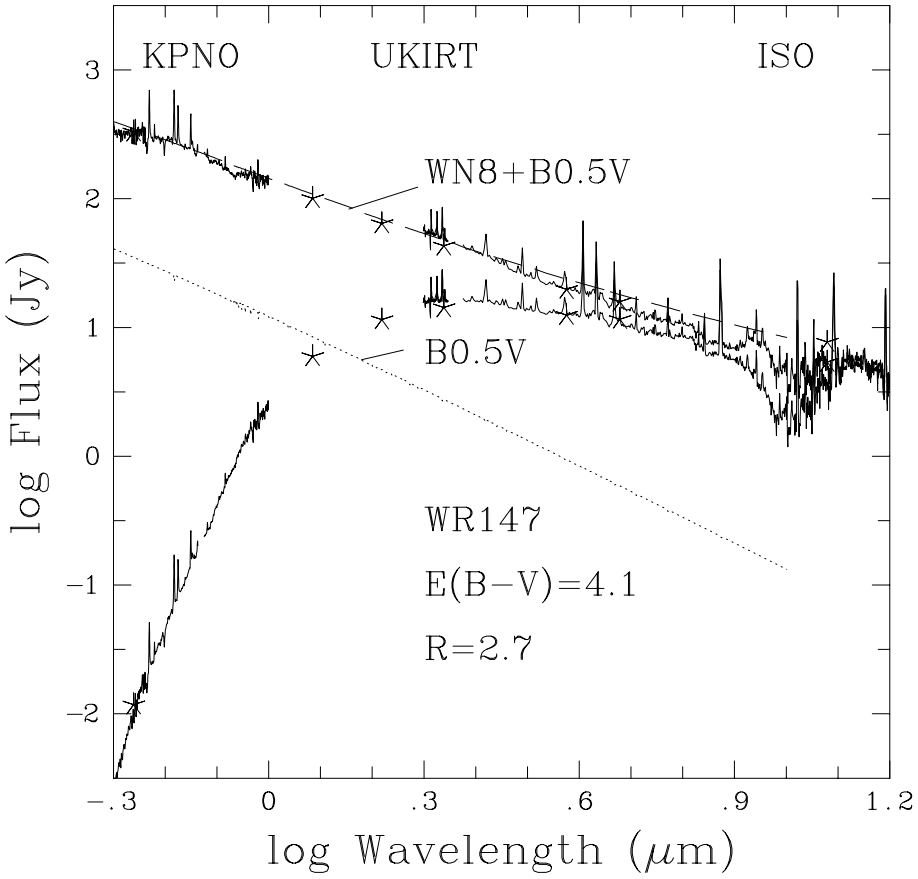

Fig. 1. Comparison between the observed, and de-reddened optical (KPNO), near-IR (UKIRT) and mid-IR (ISO) spectrophotometry of WR147 (solid lines) with the theoretical WN+O flux distribution (dotted: B0.5V, dashed: WN8+B0.5V). Near-IR photometry (stars) is taken from C92. Optical and near-IR fluxes are dereddened by $E_{\rm B-V}$=4.1 using the Cardelli et al. (1989) law, with $R_{\rm V}$=2.7, while ISO-SWS fluxes are dereddened with the curve of Cohen (priv. comm.), normalized at A_λ/A_V.

ing the de-reddening, R_V was allowed to vary in the optical and near-IR, and the Cohen curve was normalized to the final Cardelli et al. curve at 3 μm.

The best match between our theoretical flux distribution and the de-reddened optical and near-IR fluxes was obtained for $E_{B-V} \simeq 4.1\pm0.2$ mag at $R_V = 2.7\pm0.1$ (A_V = 11.2 mag), as shown in Fig. 1. A standard value of $R_V = 3.1$ led to a marginally poorer match for $E_{B-V} \simeq 3.8$ mag (A_V = 11.8 mag). Our derived extinction values are in close agreement with previous determinations by Stickland et al. (1985) and C92. Fig. 1 shows that the WR star clearly dominates the fluxes emerging from the WR+OB system.

We have been able to derive the shape of the IR extinction curve by comparing the *SWS* spectrum to the theoretical continuum for the WN8 star. The deduced curve is shown in comparison to that provided by M. Cohen in Fig. 2, normalized to A_λ/A_V by including the flux-calibrated optical data de-reddened with the R = 2.8 extinction curve of Cardelli et al. (1989) and $E_{B-V} = 4.1$ mag. Differences between the two curves are apparent at $\lambda > 5$ μm, particularly where the 9.7 and 18 μm silicate bands occur, suggesting abnormal composition of the absorbing bands.

Surprisingly, the shape of the 9.7 μm absorption band in the WR 147 spectrum is quite similar to that observed in the *SWS* spectrum of WR 112 (Fig. 3), a WC9 star with a shell of carbonaceous dust formed in the star's wind (Williams et al. 1987; van der Hucht et al. 1996). The large extinction of radiation from the WC star ($A_V \simeq 11.9$ mag) is believed to occur only partially in the circumstellar shell, with additional extinction by cooler material in the local environment, producing a 10-μm absorption band that is deep ($\tau_{9.7} \simeq 0.64$; van der Hucht et al. 1996) and markedly narrower than normally seen in the ISM (see the representative band in the spectrum of Galactic Centre source GSC 3 in Fig. 3). The unusually high optical depth at the A_V of WR 112 has been suggested to indicate the presence of cooler material possibly shed during the red supergiant phase. The presence of local, but cool, environmental dust left over from a previous evolutionary phase could explain the high extinction towards WR 147, but the profile shapes seen in both WR 147 and WR 112 deviate from those seen in the shells of red supergiants such as NML Cyg and IRC+10 420, indicating differences in grain chemistry or clustering properties. Given the peculiar profile shape, the close proximity of the system (Sect. 2.4), and the lack of any ice features in the SWS spectrum to indicate the presence of intervening cold molecular material, we doubt that the material in front of WR 147 is located in the foreground ISM. Conversely, the material cannot be warmed, since we detect no thermal emission at wavelengths to 45 μm.

Is this material the dust created in a high-density outflow during an LBV phase? In addition to the lack of thermal emission, we can find no similarities with any of the observed dusty LBV nebulae, since no nebulosity near WR 147 is indicated in H α and [O III] λ5007 imaging at $\sim 1''$ spatial resolution (Miller & Chu 1993). This is consistent with the absence of nebular lines

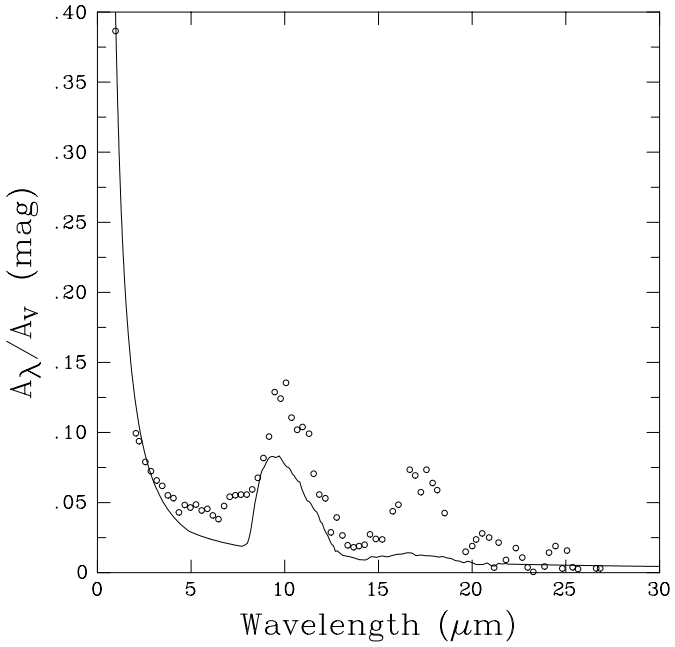

Fig. 2. Form of IR extinction curve for WR 147 (open dots), assuming that both the theoretical WR flux distribution and *ISO* flux calibration are appropriate, compared with the curve of Cohen (solid line), normalized to A_λ/A_V.

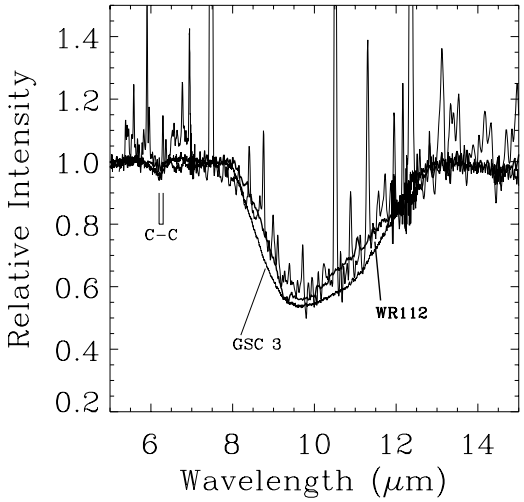

Fig. 3. Normalized spectra of WR 147 (exhibiting the emission lines), WR112 (thick), and Galactic Centre source GSC 3 centered on the 10-μm absorption bands. The GSC 3 spectrum has been scaled to match the depth of the WR 147 absorption at 9.7 μm, the WR112 spectrum is unscaled. The narrow feature at 6.2 μm in WR112, GSC 3, and possibly WR 147 is attributed to C-C stretching mode of aromatics in the ISM (Schutte et al. 1998).

in the combined spectrum. The material *behaves* spectroscopically as cool circumstellar material, but the true location and origin of the intervening dust remain a puzzle.

2.4. Distance to WR 147

A distance of 630 parsec was derived by C92, who assumed that the absolute HKL' magnitudes of the WN8 star should be identical to those of WR105, believed at that time to be the only WN8 star with membership in a Galactic association (Sgr OB1; Lundstrom & Stenholm 1989). The absolute K magnitude of WR105[2] was determined by C92 to be $M_K = -5.96$ mag. Since the dispersion of absolute magnitudes in the WR subtypes can be large (e.g., van der Hucht et al. 1988; Hamann & Koesterke 1998b), we prefer to adopt an average value of $M_K = -6.2 \pm 0.3$ mag for WR 147, based on $M_K = -6.5$ mag for the LMC WN8 star HD33133 (Crowther & Smith 1997) and the M_K of WR105. Our derived extinction for WR 147 implies $A_K = 1.27 \pm 0.05$ mag. Using $m_K = 4.15 \pm 0.03$ mag taken from C92, the resulting distance modulus for WR 147 is 9.08±0.04, or $d = 650^{+130}_{-110}$ pc. The chief source of uncertainty on the distance is in the range of M_K represented by WR105 and HD33133. At 650 pc, the projected 0.″64 separation between WR 147N and WR 147S (W97; Niemela 1998) corresponds to a lower-limit physical separation of 420 AU.

The absolute visual magnitude of the system is $M_V = -6.4$ mag, and individual components have M_V(WN8) = −6.3 mag and M_V(B0.5 V) = −4.1 mag. Assuming $T_{\rm eff}$(B0.5 V)=28.5 ± 2 kK from Crowther (1997), its bolometric luminosity is log($L/\mathrm{L}_\odot$) = 4.7 ± 0.1 and its stellar mass is 15−20 $\mathrm{M}_\odot$, supporting the estimate by W97.

[2] WR105 has been reclassified as WN9h by Smith et al. (1996).

3. Spectroscopic results

The model calculations are based on the iterative technique of Hillier (1987, 1990) which solves the transfer equation in the co-moving frame subject to statistical and radiative equilibrium, assuming an expanding, spherically-symmetric, homogeneous and static atmosphere. Allowance is made for line blanketing and clumping following the formulation of Hillier & Miller (1998,1999). The stellar radius (R_*) is defined as the inner boundary of the model atmosphere and is located at Rosseland optical depth of ∼20 with the stellar temperature (T_*) defined by the usual Stefan-Boltzmann relation. Similarly, the effective temperature ($T_{\rm eff}$) relates to the radius ($R_{2/3}$) at which the Rosseland optical depth equals 2/3.

A simplifying 'super level' approach is used for individual levels (Anderson 1989), particularly for iron-group elements. In this approach, several levels of similar energies and properties are treated as a single 'super level', with only the populations of the super level included in the solution of the rate equations. The population of an individual atomic level in the full model atom is determined by assuming that it has the same departure coefficient as the corresponding super level to which it belongs.

The final model atom contains hydrogen, helium, carbon, nitrogen, silicon and iron as shown in Table 1. Weak transitions of iron ($gf \leq 10^{-4}$) have been excluded. In total, 307 super levels, 1085 full levels and 10,145 non-LTE transitions are simultaneously considered. Elemental abundances other than hydrogen and helium are fixed at cosmic (Si = 0.1% by mass, Fe = 0.2%

Table 1. Summary of model atom used in calculations, including full ($N_{\rm F}$), and super ($N_{\rm S}$) levels and number of transitions ($N_{\rm Trans}$), following the approach of Hillier & Miller (1998).

Ion	$N_{\rm S}$	$N_{\rm F}$	$N_{\rm Trans}$	Details
H I	10	30	435	$n \leq$30.
He I	42	69	905	$n \leq$20.
He II	13	30	435	$n \leq$30.
C III	21	38	147	$nl \leq$2s4f^{1}F$^\circ$
C IV	9	14	48	$n \leq 4$.
N II	23	41	144	$nl \leq$2p3d^{1}P$^\circ$
N III	33	48	407	$nl \leq$2p4p^{2}D
N IV	22	38	144	$nl \leq$2p3d^{1}D$^\circ$
Si III	25	45	170	$nl \leq$3s5f^{1}F$^\circ$
Si IV	17	28	129	$n \leq 6$.
Fe III	52	242	1840	$nl \leq$3d^5(^{4}F)5s^{5}F
Fe IV	21	280	3538	$nl \leq$3d^4(^{1}G)4p^{2}P$^\circ$
Fe V	19	182	1803	$nl \leq$3d^3(^{2}D)4p^{1}P$^\circ$
	307	1085	10145	

Table 2. Principal ($\geq$1% of total line equivalent width, EW) transitions contributing to the 7.4$-$7.5 μm complex, including approximate EWs. He I states for $n \leq 7$ and $l \geq 3$ are grouped into a single Z state. He I makes a major contribution to the mid-IR hydrogenic features, but note that EWs cannot be summed directly due to interactions between line components.

Ion	Transition	λ (μm)	EW (Å)
He I	$6z^3Z-5{\rm d}^3D$	7.4300	67
He I	$6z^1Z-5{\rm d}^1D$	7.4300	69
He I	$6z^3Z-5{\rm z}^3Z$	7.4536	457
He I	$6z^1Z-5{\rm z}^1Z$	7.4536	333
H I	6$-$5 (Pf α)	7.4578	502
He I	$8z^3Z-6{\rm d}^3D$	7.4819	30
He I	$8z^3Z-6{\rm z}^3Z$	7.4966	176
He I	$8z^1Z-6{\rm z}^1Z$	7.4966	60
H I	8$-$6 (Hu β)	7.5004	133
He I	11$-$7	7.5026	60
H I	11$-$7	7.5061	34

by mass) or CNO-equilibrium (C = 0.03% by mass, N = 1% by mass) values for a solar metallicity environment.

Our approach follows that of Crowther et al. (1995b), such that diagnostic optical lines of He I (λ5876), He II (λ4686) and H I (Hβ+He II λ4859) are chosen to derive the stellar temperature, mass-loss rate, luminosity and hydrogen content. The mass-loss rate is actually derived as the ratio $\dot{M}/\sqrt{f}$, where f(opt-IR) is the volume filling factor that can be constrained by fits to the electron scattering wings of the helium line profiles. The quality of the *ISO-SWS* data is sufficient that we could readily select IR line diagnostics (e.g. He I 4.29μm, He II 3.09μm, Brβ). However, we adhere to optical diagnostics in order to provide consistency with previous quantitative studies of WNL stars. A terminal wind velocity, v_∞, of 950 km s^{-1} is obtained from optical He I P Cygni line profiles and the mid-IR fine structure lines of [S IV] and [Ne III]. This value is consistent with previous studies: Eenens & Williams (1994) obtained 1,100 km s^{-1} from He I 1.083μm spectroscopy, while Hamann et al. (1995) estimated 1000 km s^{-1} from optical spectroscopy. The form of the velocity law of WR stars is taken to be $v(r) = v_\infty(1 - R_*/r)^\beta$, where β is indicated to be in the range of 5 to 10 for WR stars with very extended line-forming regions (cf. Hillier & Miller 1999; Lépine & Moffat 1999), and is probably more modest for the weaker-lined WNL stars. We have compared predictions with β = 1 and β = 2 laws.

3.1. Stellar properties of the WN8 star

Rectified optical and near-IR spectroscopy of WR 147 are compared to our synthetic spectra in Fig. 4. The main transitions are identified. Overall, agreement is excellent except for a few notable exceptions. He I 2.06μm emission is too weak, although this is known to be extremely sensitive to the precise EUV flux distribution (Najarro et al. 1994, 1997, 1998a,b; Crowther et al. 1995b), while N IV emission at λ4058 and $\lambda\lambda$7103-29 is not predicted. In Fig. 5 we compare the predictions of this model with our rectified *ISO-SWS* data set. [An extensive list of the (probable) contributing transitions is provided in the Appendix.] Agreement is again excellent, except for He II λ3.09μm (too weak), Brα (too strong). In many cases, the observed profile is blend of many transitions, with He I and H contributing equally. To illustrate this, we list the principal contributors to the H+He I complex at 7.4$-$7.5 μm in Table 2, and compare the observed and synthetic profiles in Fig. 6.

The stellar parameters derived for the WN8 star are presented in Table 3. These are typical of other WNL stars (Crowther et al. 1995a), with H severely deficient, but definitely present at $\sim$9% by mass. This confirms the WN8(h) classification by Smith et al. (1996). We compare our results to the study by Hamann et al. (1995), who used optical hydrogen and helium lines.[3] Their approach was identical except that line blanketing and clumping was neglected in their study. Hamann et al. derived slightly lower hydrogen content, 5% by mass, but values for the stellar and wind parameters are otherwise similar to our results. This indicates that the neglect of line-blanketing does not (at least in the case of WR 147) seriously affect the accuracy of the derived quantities. The chief difference in the values of $\dot{M}$, which is $\sim$3 times lower according to our analyses, is understood as a result of the low volume filling factor of f(opt-IR) = 0.1, needed to achieve good fits to the electron scattering wings of the He emission line profiles. In Fig. 7 we compare optical line profiles predicted by homogeneous and clumped models of identical parameters except for mass-loss, with He II λ5412 Å and λ3.0908 μm observations. Clearly, the homogeneous model overestimates the red electron scattering wings, though the quality of the observational data is not sufficient to derive a unique filling factor. A filling factor in the range of 0.04 to 0.25 is consistent with observations, so that the possible mass-loss rate is a factor of between 2 and 5 times lower than the homogeneous solution, now spanning the range

[3] Hamann & Koesterke (1998b) have recently obtained slightly revised parameters based on nitrogen diagnostics.

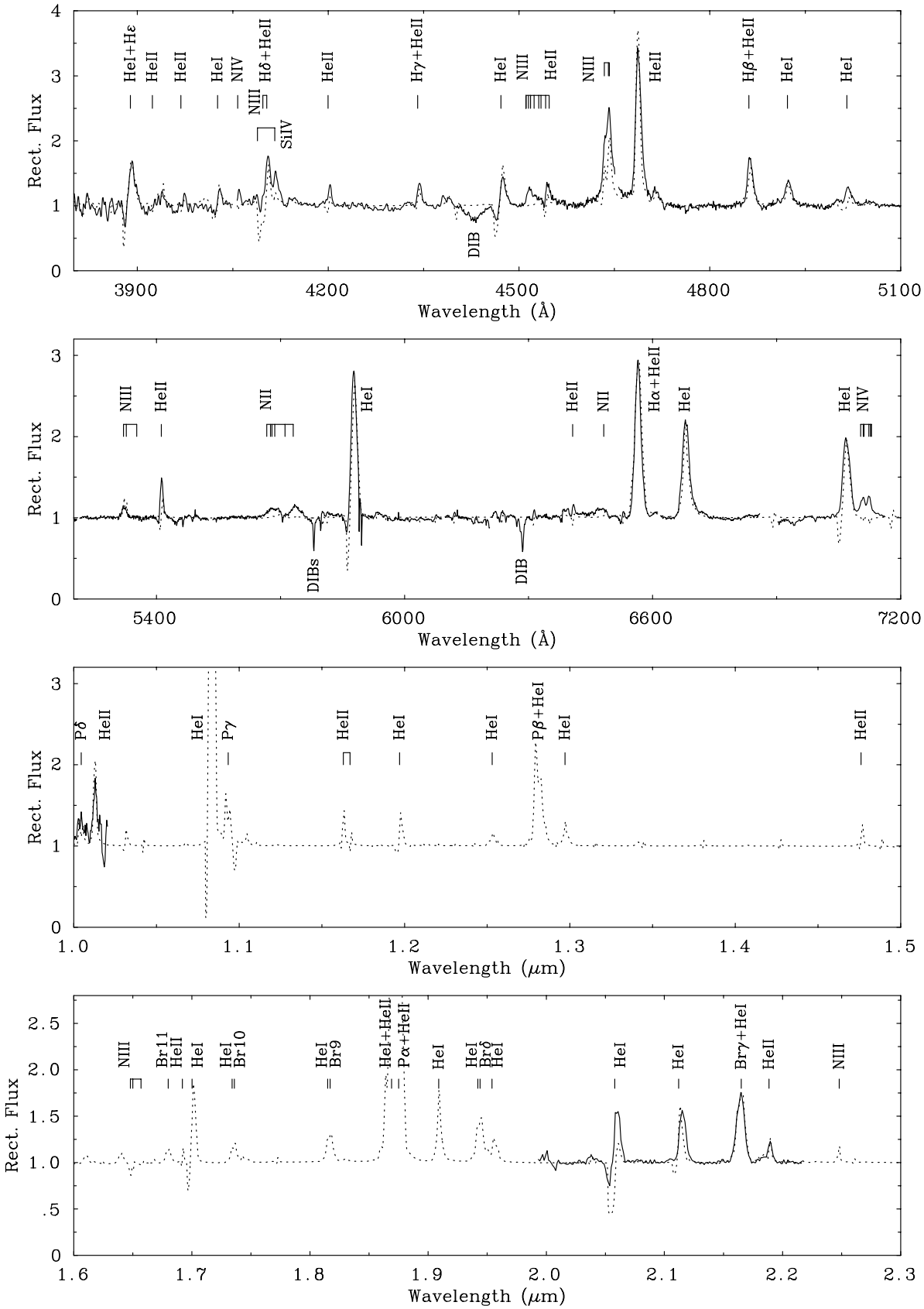

Fig. 4. Comparison between the optical (INT) and near-IR (UKIRT) rectified spectrum of WR 147 (solid lines) with our synthetic WN8 + OB spectrum. The predicted peak intensities of He I 1.083μm and Pα reach 9.1 and 5.3 times the local continuum.

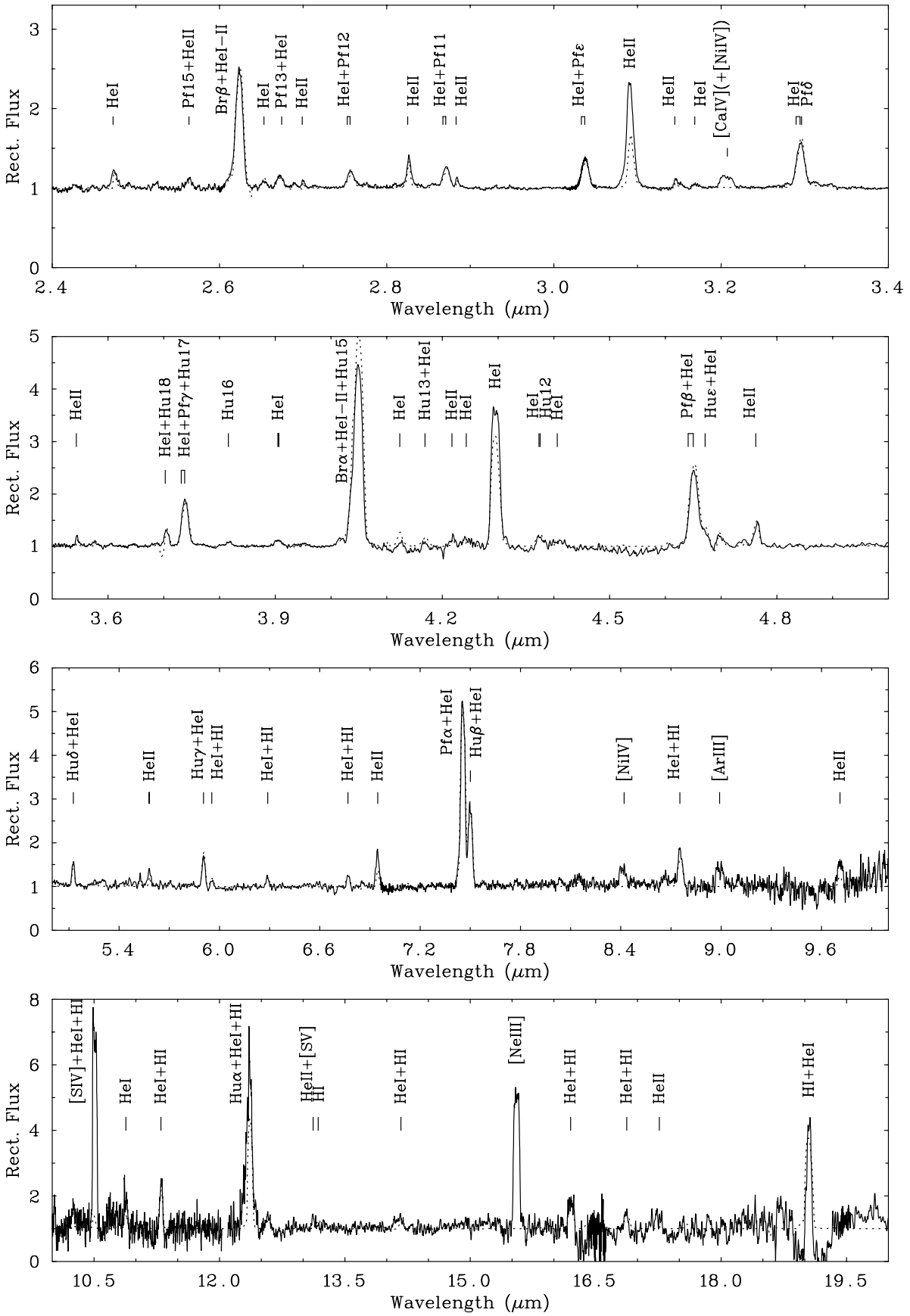

Fig. 5. Comparison between the mid-IR *ISO-SWS* rectified spectrum of WR 147 (solid lines) with our synthetic WN8 + OB spectrum.

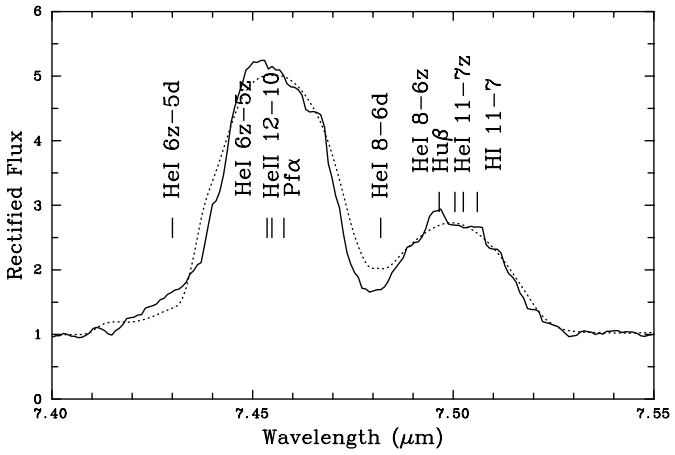

Fig. 6. Comparison between the synthetic profile around Pf α (dashed) and the *SWS* observations (solid). Lines contributing to the synthetic profile are indicated (see also Table 2).

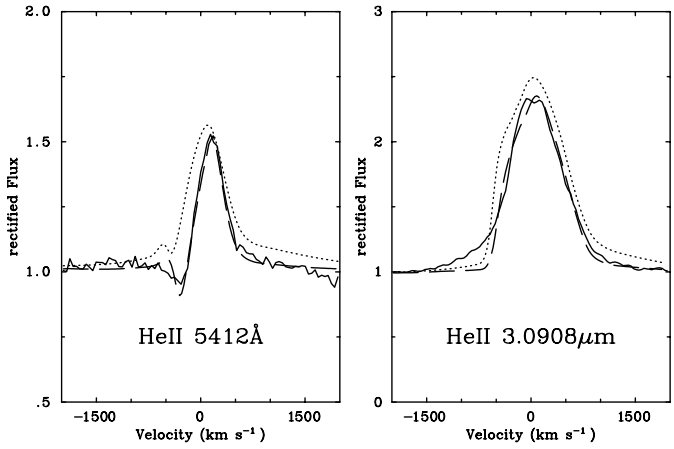

Fig. 7. Comparison between line profiles obtained from smooth (dotted) and clumped (dashed) models of WR 147, together with INT observations (solid). Our clumped model assumes a volume filling factor of 10%.

of $(1.5-3.7)\times10^{-5}$M$_\odot$ yr^{-1}. The contrast between synthetic profiles obtained from homogeneous and clumped models diminishes towards longer wavelengths, but ideally we could use the optical-IR continuum distribution to test various clumping factors and/or the value of β (as done, e.g., with the optical-IR spectrum of P Cyg by Lamers et al. 1996; see also Najarro et al. 1998a,b) This is prevented, however, by uncertainties in the correction for extinction towards WR 147 (Sect. 2.3). Consequently, the value of $\dot{M}$ is uncertain by ∼50%. Nevertheless, the well known wind performance factor, $\dot{M}v_\infty/(L_*/c)$, is reduced from 10 (Hamann et al. 1995) to ∼2.5.

C92 measured the 6cm (4.8GHz) radio flux of WR 147S with the VLA at finding 21.4 and 19.4mJy between 1984 September and 1985 January, while Contreras & Rodríguez (1999) measured an increase in the 3.6cm (8.1GHz) flux of WR 147S from 25.5mJy in 1995 July to 31.3mJy in 1996 December. We can predict the expected radio flux obtained from our derived mass-loss rate by using the form of the Wright & Barlow (1975) formula presented by Leitherer et al. (1997) or Hillier & Miller (1999). Assuming dominant ionization states of H^+, He^+ and N^{2+}, and T_e = 9,400 K from C92, we obtain values for the mean ionic weight, μ = 3.18, mean number of electrons per ion, γ_e = 1.003, and RMS ionic charge, z = 1.005. The predicted flux further depends on the volume filling factor for for the radio forming region (at around $\sim800R_*$) as illustrated in Table 4. We find that the mass-loss rate derived from optical/IR recombination lines is consistent with the radio flux if the filling factor at high wind densities ($\sim10^{11}$ cm^{-3}) is a factor of two smaller than at low densities ($\sim10^5$ cm^{-3}). Radio observations (W97; Contreras & Rodríguez 1999) favour filling factors of f(radio)∼0.1, which would suggest f(opt-IR) = 0.04 or $\dot{M}$ = 1.5×10^{-5}M$_\odot$ yr^{-1}.

3.2. Elemental abundances: Ne, S, Ca

The surface abundances of elements with IR fine structure lines formed in the outer regions of the WN8 star wind can be estimated following the technique of Barlow et al. (1988, hereafter B88). An analytical expression for the ion number fraction γ_i was derived by B88. This expression, adapted to allow for clumping in the wind, has the form

$$\gamma_i = C(T_e)\frac{d^2 I_{ul}\sqrt{f}}{\gamma_e^{1/2}A^{3/2}h\nu_{ul}}T_e^{1/4}e^{h\nu_{ul}/kT_e}$$

where d is the stellar distance, I_{ul} is the line flux of the transition with energy $h\nu_{ul}$ between upper level u and lower level l, γ_e and

Table 3. Comparison of stellar parameters for WR 147 (WN8) derived here (labeled 'Model') with those determined previously by Hamann et al. (1995, HKW95) and Hamann et al. (1998b, HKW98), scaled to our absolute magnitude*.

Analysis	T_*	R_*	$\log L_*$	$\log(\frac{\dot{M}}{\sqrt{f}})$	f	v_∞	$\frac{\rm H}{\rm He}$	M_v
	kK	R$_\odot$	L$_\odot$	M$_\odot$/yr		km/s		mag
Model	32.9	20.6	5.65	−4.1	0.1	950	0.4	−6.3*
HKW95	31.5	21.2	5.60	−4.1	1.0	1000	0.2	−6.3
HKW98	35.5	18.9	5.71	−4.4	1.0	1000	0.2	−6.3

* Our analysis assumes M_K = −6.2 mag. M_v results from our predicted theoretical continuum distribution. The parameters determined by Hamann et al. (1995, 1998b) have been rescaled to this value of M_v.

Table 4. Comparison between predicted and observed radio fluxes for various mass-loss/filling factor combinations. Observed fluxes are from C92 at 6 cm and Contreras & Rodríguez (1999) at 3.6 cm.

$\dot{M}_{\rm spect}$	f	f	$S_\nu^{3.6\rm cm}$(mJy)		$S_\nu^{6\rm cm}$(mJy)	
M$_\odot$ yr^{-1}	(opt-IR)	(radio)	Pred.	Obs.	Pred.	Obs.
1.5×10^{-5}	0.04	0.08	29	25–31	21	19–21
2.4×10^{-5}	0.10	0.04	85	25–31	62	19–21
2.4×10^{-5}	0.10	0.10	46	25–31	34	19–21
2.4×10^{-5}	0.10	0.25	25	25–31	18	19–21
3.7×10^{-5}	0.25	0.50	29	25–31	21	19–21

Table 5. Observed line intensities (de-reddened) and atomic parameters. Statistical weights of upper and lower levels are ω_u and ω_l, the transition probability is A_{ul}, the Maxwell average collision strength is $\Omega_{ul}(T_e)$, and critical upper level density is $n_c(u)$. Ω_{ul} and $n_c(u)$ are given at T_e = 9000 K.

Ion	Transition	λ (μm) vacuum	observed	ω_u	ω_l	A_{ul} (s^{-1})	Ref	$\Omega_{ul}(T_e)$	Ref	$n_c(u)$ (cm^{-3})	Intensity (W m^{-2})	E.W. (Å)
[Ca IV]	$^2P^\circ_{1/2}$–$^2P^\circ_{3/2}$	3.2067	3.207	2	4	5.43×10^{-1}	a	0.97	b	1.231×10^{7}	1.01×10^{-14}	24
[S IV]	$^2P^\circ_{3/2}$–$^2P^\circ_{1/2}$	10.5105	10.506	4	2	7.70×10^{-3}	a	8.52	c	5.330×10^{4}	1.59×10^{-14}	3250
[Ne III]	$^3P^\circ_1$–$^3P^\circ_2$	15.5550	15.558	3	5	5.99×10^{-3}	a	0.77	d	1.788×10^{5}	1.36×10^{-14}	3190

(a) Naqvi (1951); (b) Pelan & Berrington (1995); (c) Saraph & Storey (1999); (d) Butler & Zeippen (1994);

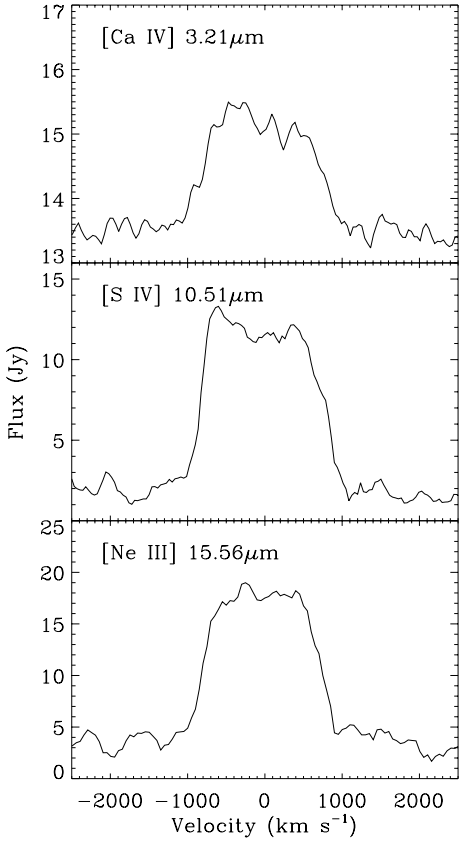

Fig. 8. Mid-IR fine structure transitions of Ca IV, S IV, and Ne III observed with *ISO-SWS*. Half-widths at zero intensity indicate a terminal wind velocity of $v_\infty \simeq 950$ km s^{-1}.

T_e are the electron number density and temperature in the line-forming region, $C(T_e)$ are the atomic constants which include a weak temperature dependence (mainly through the upward and downward collision rates), and A is a mass-loss parameter. This mass-loss term is defined by B88 as

$$A \equiv \dot{M}/4\pi\mu m_{\rm H} v_\infty.$$

Note that the scaling $\gamma_i \propto \sqrt{f}/\dot{M}^{3/2}$ from the above equations implies that the ion fractions γ_i are indeed sensitive to wind clumping. For example, a filling factor of 4% leads to a mass-loss rate of 1.5×10^{-5} $M_\odot$ yr^{-1}, which is 5 times lower than the case of a homogeneous wind, and the net effect on γ_i is to increase it (relative to a homogeneous wind) by a factor of $\sim$2.3. We must caution, however, that since the fine structure lines are formed in the outer regions of the wind extending into the constant velocity regime where densities are low, the volume filling factor may be considerably different than estimated from the optical and near-IR recombination lines. From our spectroscopic mass-loss results, we provide estimates of γ_i assuming clumping factors of f(opt-IR) = 0.04, 0.1 or 0.25.

The fine structure lines of [Ca IV] 3.21μm, [Ne III] 15.55μm, and [S IV] 10.5μm are shown in Fig. 8. The de-reddened line fluxes and atomic quantities used to estimate the ion fractions are listed in Table 5. Transition probabilities are taken from the NIST Atomic Spectra Database, while collision strengths are obtained from papers in the IRON Project series. Ion fractions for Ne^{2+}, S^{3+}, and Ca^{3+} are estimated at representative densities of 10^5 cm^{-3} (neon and calcium) or 10^4 cm^{-3} (sulphur). This region corresponds to a physical radius of 300–1000 AU, or $\sim$3,000–10,000R_*(WN8), i.e., a flow timescale of several years at the terminal wind velocity of 950 km s^{-1}.

In addition to the analytical two-level expression for the determination of γ_i, Dessart et al. (1999, in prep.) have updated the method of B88 in which an integration is performed over the entire density range to take account of clumping. We present abundances derived from both the analytical and integral techniques in Table 6, for a variety of mass-loss rates and filling factors for neon, sulphur, and calcium. We find that abundances derived from the analytical expression for [Ca IV] are in excellent agreement with the integral method, while [Ne III] and [S IV] are systematically too high by $\sim$20% and up to 50%, respectively. Only a few percent of the [Ne III] overestimate is due to the fact that the 15.55 μm transition is actually split into three levels rather than two, but the [S IV] 10.51 μm line is split into only two fine structure levels and the large overestimate is accounted for in the integration over the full range of wind densities where line-formation occurs.

We do not make corrections for unseen ionization stages, noting that both [S III] 18.7μm and [Ne II] 12.8μm are absent. We do not expect [Ne IV] (IP = 97eV) emission to occur, since [Ca V] 4.15μm is absent (IP of 84eV), although some sulphur may exist in [S V] (IP of 73eV). Consequently, the neon abundance derived from the observed ionic transitions should be fairly representative of the total elemental abundance. The situation is less straightforward for sulphur and especially for calcium, since no transitions of [Ca III], expected to be the dominant ionization stage (IP = 51eV) occur in the visible or IR. The

Table 6. Summary of elemental abundances obtained from mid-IR fine structure [Ne III], [S IV] and [Ca IV] transitions, using mass-loss rates obtained from optical-IR spectroscopy. All calculations were performed at T_e = 9400 K, and assume an ionization balance of singly ionized H and He, and doubly ionized nitrogen. We show γ_X obtained from analytical and integral techniques, while the latter is preferred for our final abundances. Cosmic abundances for the H-depleted atmosphere of WR147 are shown in parenthesis.

Element (cosmic)	$\dot{M}$ $M_\odot$ yr^{-1}	f	γ_X(anal.) 10^{-5}	γ_X(integ.) 10^{-5}	X/He 10^{-5}
Neon	1.5×10^{-5}	0.04	22.8	19.2	26.9
(34×10^{-5})	2.4×10^{-5}	0.10	18.2	15.3	21.4
	3.7×10^{-5}	0.25	14.4	12.2	17.1
Sulphur	1.5×10^{-5}	0.04	3.07	2.08	2.91
(5.1×10^{-5})	2.4×10^{-5}	0.10	2.44	1.65	2.31
	3.7×10^{-5}	0.25	19.4	1.31	1.83
Calcium	1.5×10^{-5}	0.04	0.40	0.37	0.52
(0.7×10^{-5})	2.4×10^{-5}	0.10	0.32	0.30	0.42
	3.7×10^{-5}	0.25	0.25	0.24	0.34

outer wind ionization state and electron temperature have negligible influence on the elemental abundances, unless helium is neutral (which is unlikely), in which case abundances that are a factor of twenty times higher are obtained. In the case of neon, Ne^{2+}/He = (1.7 to 2.7)$\times10^{-4}$, from our spectroscopic mass-loss rate, which compares favourably with the solar value of Ne/He = 3.4×10^{-4} for the H-depleted environment of WR147. Therefore, in contrast with previous results by Morris et al. (1998), we do *not* find a higher neon abundance for WR 147 than is expected for unprocessed material in a solar-type environment. We return to this discrepancy in Sect. 4.

In the case of sulphur, S^{3+}/He = (1.8 to 2.9)$\times10^{-5}$, from our spectroscopic mass-loss rate, which given the uncertain contribution of S^{4+} compares favourably with the solar value of S/He $\simeq 5\times10^{-5}$ for the H-depleted environment of WR 147. Similarly for calcium, we obtain Ca/He $\geq$ (3 to 5)$\times10^{-6}$ which is in reasonable accord with the anticipated abundance of Ca/He = 7×10^{-6} by number, again considering that calcium may also be present in Ca^{2+}.

Since the method of B88 applied here to estimate abundances of elements in the ratio with helium depends strongly on the values of $\dot{M}$ and f, Ne^{2+}/S^{3+} and Ne^{2+}/Ca^{3+} should provide more reliable abundance ratios than Ne/He, S/He, or Ca/He. We find in all cases Ne^{2+}/S^{3+} = 9 and Ne^{2+}/Ca^{3+} = 50 in excellent agreement with the expected ratios of Ne/S = 7 and Ne/Ca = 50.

4. Summary and conclusions

Combined optical, near-IR and ISO-SWS infrared spectrophotometry of the WN8 + OB binary WR 147 have been analyzed using non-LTE methods to deduce the physical properties of the WN8 star. The assumption of wind homogeneity has been relaxed, warranted by strong observational evidence for clumping in the winds of WN8 stars as the most spectroscopically and photometrically variable among WR subtypes, and by the evidence for clumping from radio observations of WR147 in particular. Our analyses represent the first detailed spectroscopic study of a WN8 star using a wind model that incorporates clumping and line blanketing, and the first to include mid-infrared spectroscopy. The results can be summarized as follows:

1. *Extrinsic observables.*
   Extinction. The best fit between the observed optical to near-IR flux distribution (de-reddened using curves of Cardelli et al. 1989 at different values of R_V) and our theoretical energy distribution leads to a colour excess E_{B-V} of 4.1 mag at R_V = 2.7 (A_V = 11.2 mag). These are in good agreement with previous estimates. The value of R_V indicates extinction properties that are atypical of dust in the ISM. This is clearly underscored by the mid-IR extinction curve we derived from the *ISO-SWS* spectrum, which deviates from an average ISM extinction curve at $\lambda > 5\,\mu$m, especially in the silicate bands at 10 and 18 μm. The nature of the extinction is very puzzling due to (i) the atypical shape of the 10 μm absorption profile, and (ii) the close proximity of the system.
   Distance. Using WR105 (WN9h) and HD33133 (WN8h) as calibrators in the K band, we obtain a distance of 650 pc to WR147, in good agreement with C92. The absolute visual magnitude of the system is $M_V = -6.4$ mag, and individual components have M_V(WN8) = -6.3 mag and M_V(B0.5V) = -4.1 mag, and are presently separated by 420 AU. We derived the bolometric luminosity and stellar mass of the B0.5V star, confirming estimates by W97.
2. *Clumping.*
   Due to the paucity of spectroscopic observations of WR 147, variability of line profile substructures (that would provide definitive evidence for wind clumping; cf. Moffat et al. 1988) could not be searched for. Static optical and mid-IR line profiles, however, exhibit excesses of flux in the red electron scattering wings. A filling factor f of 0.1 achieves good agreement between observed and synthetic profiles (emphasizing the scattering wings), but values between 0.04 and 0.25 are very acceptable. The value of f or β (in the velocity law) could not be tuned with the overall optical-IR distribution due to reddening uncertainties. Nonetheless, the preference on f is towards the lower end on the basis of comparison between observed radio fluxes and those predicted over the range of $\dot{M}/\sqrt{f}$, leading to f(opt-IR) $\simeq$ 0.04, f(radio) $\simeq$ 0.1, and $\dot{M} \simeq 1.5\times10^{-5}$ $M_\odot$ yr^{-1}, taking the lower wind density of the radio-emitting regime into account. This mass-loss rate is approximately 2.5 to 5 times lower than estimated from radio observations and optical spectroscopy on the assumption that f = 1.0.
3. *Line blanketing.*
   The inclusion of blanketing by metal ions may have contributed to lowering the derived mass-loss rate by altering the ionization structure and individual line strengths. The bolometric luminosity is not substantially altered, in agreement with tests of other WNL stars (Herald et al. 1999), so that the performance number $\dot{M}v_\infty/(L_*/c)$ is reduced

from about 10 (Hamann et al. 1995) to ∼2.5 mainly as a consequence of allowing for clumping.

4. *Elemental abundances*.
Hydrogen is found to be present at 9% by mass from the best-fit wind model. Fine structure lines of [Ca IV], [S IV], and [Ne III] in the ISO-SWS spectrum were used to estimate surface abundance ratios of these elements, using an integration technique developed by Dessart et al. (1999, in prep.) that follows the basic approach by B88 for normalization by the mass-loss rate. In the ratio with He, the abundances are in good agreement with cosmic values for the H-depleted environment of WR 147S. Small differences are probably due to uncertainties on the value of $\dot{M}$ and f rather than our neglect of unseen ionization stages, since ionization potentials of the observed ionization stages make others somewhat unlikely, whilest Ne/Ca and Ne/S (which divides out the $\dot{M}$ uncertainty) are in excellent agreement with cosmic values.

In conclusion, the sensitivity of the derived value of the mass-loss rate to clumping can have a significant impact on the testing of evolutionary predictions. In relation to this study, abundances of ^{22}Ne are predicted (Maeder 1991) to reach two orders of magnitude over the solar value at the surfaces of Galactic WC stars through a chain of core nucleosynthesis reactions involving α-capture by ^{14}N, β-decay of ^{18}F, and α-capture by ^{18}O. No Ne production is involved in the CN or ON branches of the CNO cycle, and thus Ne enhancements are not expected at the surfaces of WN stars. These stars tend to show CNO-equilibrium surface abundances (e.g., Willis 1991), understood to be the result of mass-loss that uncovers the CNO-processed layers of the core. Most recently, however, Meynet (1999) and Maeder (1999) have presented new models of massive rotating stars that indicate a strong influence on the surface abundances and lifetimes of WN stars by diffusive mixing related to shear instabilities. The results show that enhancements of N (a product of H-burning) may be observed simultaneously with C and Ne enhancements (He-burning products), suggestive of the WN/WC transition stars (Meynet 1999). No WN/WC stars with flux levels within the range of *ISO-SWS* sensitivities could be observed to investigate the Ne abundances in this transition phase, but Morris et al. (1998) had reported indications of Ne enhancement (roughly factor of two above expectations) at the surface of WR 147S, a possible result of rotational mixing. The estimate relied on literature values of the mass-loss rate for the WN8 star, which to this point have been determined under the assumption of homogeneity. While it was emphasized that the overabundance is within the range of corresponding mass-loss rate uncertainties (see especially Morris et al. 1999), the results of this study resolve the overabundance as an overestimate arising from the neglect of clumping.

The consequences of this study on testing the latest evolutionary abundance predictions, then, are two-fold: (1) allowances must be made for inhomogeneities in WR winds to reach a more reliable assessment of surface abundances in formalisms that strongly relies on the value of the mass-loss rate; and (2) The normal Ne abundance at the surface of the WN8 star provides an endorsement that advanced burning products are not exposed via rotational mixing prior to the WN/WC or WC stages.

Acknowledgements. The authors express their gratitude to Dr. M. Cohen for useful comments and the unpublished IR extinction curve, and to Dr. A.F.J. Moffat and our referee Dr. I. Stevens for helpful remarks. The authors have made use of atomic line lists compiled by Dr. P. van Hoof. PWM acknowledges financial support from a *Pionier* grant by the Netherlands Organization for Scientific Research (NWO). PAC is in receipt of a Royal Society University Research Fellowship.

Appendix

Line identifications in the *ISO*-SWS 2.4 – 23 μm spectrum of WR 147 (WN8(h)+B0.5V).

Table A1. Line-identification selection criteria for the WR 147 2.4 – 23 μm spectrum, based on examination of its *ISO-SWS* AOT-1 (speed 3) and AOT-6 spectra.

H I series	
n-4 (Brackett)	present
n-5 (Pfund)	present till $n = 22$
n-6 (Humphreys)	present till $n = 18$
n-7	present till $n = 14$
n-8	present till $n = 14$
n-9	present till $n = 14$
n-10	absent
He I series	
n-4	present
n-5	present till $n = 7$
n-6	absent unless clustering of lines $n = 7$
n-7	absent unless clustering of lines $n = 8$
n-8	absent unless clustering of lines $n = 9$
n-9	absent unless clustering of lines $n = 10$
n-10	absent
He II series	
n-6	present
n-7	present
n-8	present
n-9	weakly present
n-10	weakly present till $n = 12$
n-11	weakly present till $n = 13$
n-12	absent
forbidden lines	wavelength coincidences

Table A2. Wavelengths of observed emission features in the *ISO SWS*-AOT1/s3 and *SWS*-AOT6 spectra of WR147, compared with laboratory lines. Permitted lines: HI, HeI and HeII. Forbidden: [NeIII], [NeV], [SIV], [SV], [ArIII], [CaIV] and [NiIV]. Data from tabulation by Peter van Hoof: Atomic Line List V2.01 (23FEB99), WWWeb page <http://www.pa.uky.edu/ peter/atomic/>

AOT-1/s3		AOT-6		identification		
λ_{obs} (μm)				λ_{calc} (μm)	ion	configuration
SWS-Band 1A						Band starts at 2.37 μm
2.378	w	2.379	vw	2.3795	HeII	19 - 9
2.406	}w					
2.411	}w			2.4164	HI	21 - 5 (Pf21)
2.425	w	2.426	}w			
		2.429	}w	{2.4314	HI	20 - 5 (Pf20)
		2.450	w	{2.4490	HI	19 - 5 (Pf19)
		2.461	vw	2.4607	HeII	18 - 9
				{2.4700	HI	18 - 5 (Pf18)
2.474	}	2.474	}	{2.4734	HeI	1s.6d - 1s.4p
2.479	}	2.479	}			
		2.491		2.4953	HI	17 - 5 (Pf17)
		2.520	}w			
2.523	w	2.525	}w	2.5261	HI	16 - 5 (Pf16)
		2.555	}			
		2.558	}			
		2.564	}	{2.5642	HeII	17 - 9
				{2.5643	HI	15 - 5 (Pf15)
						Band ends at 2.61 μm
SWS-Band 1						Band starts at 2.60 μm
2.607	}w					
2.610	}	2.609	}	{2.6120	HeI	1s.6p - 1s.4d
	}	2.613	}	{2.6126	HI	14 - 5 (Pf14)
	}		}	{2.6192	HeI	1s.6f - 1s.4d
	}		}	{2.6206	HeI	1s.6f - 1s.4d
2.623	}s	2.623	}s	{2.6241	HeI	1s.6g - 1s.4f
				{2.6248	HeII	12 - 8
				{2.6254	HeI	1s.6d - 1s.4f
				{2.6259	HI	6 - 4 (Br-β)
				{2.6259	HeI	1s.6d - 1s.4f
2.652	w	2.653	w	{2.6539	HeI	1s.6d - 1s.4p
		2.667	}	{2.6679	HeI	1s.6p - 1s.4d
			}	{2.6684	HeI	1s.12d - 1s.5p
			}	{2.6707	HeI	1s.13p - 1s.5d
2.670		2.672	}	{2.6721	HeI	1s.11p - 1s.5s
				{2.6738	HeI	1s.13d - 1s.5fd
				{2.6740	HeI	1s.13d - 1s.5f
				{2.6751	HI	13 - 5 (Pf13)
				{2.6755	HeI	1s.13p - 1s.5d
		2.690	w	2.6888	HeI	1s.6s - 1s.4p
2.700	w	2.700	w	2.6998	HeII	16 - 9
2.714	w	2.713	vw			

Table A2. (continued)

AOT-1/s3		AOT-6		identification		
λ_{obs} (μm)				λ_{calc} (μm)	ion	configuration
	}	2.751	}	{2.7533	HeI	1s.12p - 1s.5d
2.756	}	2.757	}	{2.7569	HeI	1s.12d - 1s.5f
				{2.7570	HeI	1s.12d - 1s.5f
				{2.7583	HI	12 - 5 (Pf12)
				{2.7602	HeI	1s.12p - 1s.5d
				{2.7608	HeI	1s.6s - 1s.4p
		2.821	}			
2.826		2.827	}	2.8260	HeII	9 - 7
2.853	w	2.854	w	2.8550	HeI	1s.5p - 1s.4s
				{2.8673	HeI	1s.11p - 1s.5d
				{2.8677	HeI	1s.11f - 1s.5d
				{2.8686	HeI	1s.11f - 1s.5d
2.871		2.871		{2.8714	HeI	1s.11f - 1s.5g
				{2.8717	HeI	1s.11d - 1s.5f
				{2.8718	HeI	1s.11d - 1s.5f
				{2.8730	HI	11 - 5 (Pf11)
2.883	w	2.884		2.8837	HeII	15 - 9
						Band ends at 3.03 μm
SWS-Band 1D						Band starts at 3.02 μm
				{3.0323	HeI	1s.10p - 1s.5d
				{3.0335	HeI	1s.10f - 1s.5d
				{3.0338	HeI	1s.9p - 1s.5s
				{3.0345	HeI	1s.10f - 1s.5d
3.036		3.037		{3.0376	HeI	1s.10f - 1s.5g
				{3.0378	HeI	1s.10d - 1s.5f
				{3.0380	HeI	1s.10d - 1s.5f
				{3.0392	HI	10 - 5 (Pf-ϵ)
3.091	s	3.091	s	{3.0917	HeII	7 - 6
				{3.0955	HeII	11 - 8
3.146	w	3.145	}w	{3.1455	HeII	14 - 9
		3.152	}w			
		3.170	w	3.1700	HeI	1s.9d - 1s.5p
		3.199	}			
3.202	}	3.203	}			
3.208	}	3.207	}	{3.2069	[CaIV]	3s2.3p5 - 3s2.3p5
		3.211	}	{3.2102	[NiIV]	3d6.(3P2).4s - 3d6.(3P2).4s
		3.279	w	3.282	NIV	11 - 10
		3.289	}	{3.2880	HeI	1s.9p - 1s.5d
			}	{3.2907	HeI	1s.9f - 1s.5d
		3.292	}	{3.2920	HeI	1s.9f - 1s.5d
3.294		3.294	}	{3.2955	HeI	1s.9f - 1s.5g
		3.296	}	{3.2956	HeI	1s.9f - 1s.5g
			}	{3.2958	HeI	1s.9d - 1s.5f
			}	{3.2959	HeI	1s.9d - 1s.5f
		3.298	}	{3.2970	HI	9 - 5 (Pf-δ)
		3.312	w			
		3.331	w	3.3309	HeI	1s.5p - 1s.4s
		3.485	w			
						Band ends at 3.53 μm
SWS-Band 1E						Band starts at 3.52 μm
3.543		3.544	}	{3.5443	HeII	13 - 9
		3.549	}	{3.549	NV	13 - 12

Table A2. (continued)

AOT-1/s3		AOT-6		identification		
$\lambda_{\rm obs}$ (μm)				$\lambda_{\rm calc}$ (μm)	ion	configuration
		3.566	}w			
3.572	}w	3.574	}w	{3.5787	HeI	1s.8d - 1s.5p
3.580	}w	3.582	}w			
		3.605	w			
3.643	w	3.644				
		3.679	}			
		3.687	}			
		3.699	}	3.6926	HI	18 - 6 (Hu18)
3.705		3.704	}	3.7036	HeI	1s.5d - 1s.4p
		3.708	}			
		3.729	}	{3.7270	HeI	1s.8p - 1s.5d
			}	{3.7309	HeI	1s.7p - 1s.5s
			}	{3.7328	HeI	1s.8f - 1s.5d
			}	{3.7344	HeI	1s.8f - 1s.5d
3.737	s	3.737	}s	{3.7382	HeI	1s.8g - 1s.5f
			}	{3.7388	HeI	1s.8h - 1s.5g
			}	{3.7391	HeI	1s.8f - 1s.5g
			}	{3.7394	HeI	1s.8d - 1s.5f
			}	{3.7398	HeI	1s.8d - 1s.5f
		3.741	}	{3.7406	HI	8 - 5 (Pf-γ)
			}	{3.7494	HI	17 - 6 (Hu17)
		3.803	}w			
3.817	w	3.816	}w	{3.8195	HI	16 - 6 (Hu16)
				{3.9016	HeI	1s.15p - 1s.6d
3.904	w	3.906	w	{3.9058	HeI	1s.15d - 1s.6f
				{3.9075	HI	15 - 6 (Hu15)
				{3.9082	HeI	1s.15p - 1s.6d
				{3.9095	HeI	1s.14d - 1s.6p
3.947	}w					
3.958	}w					
				{4.0064	HeI	1s.5p - 1s.4d
				{4.0143	HeI	1s.14p - 1s.6d
		4.019	w	{4.0190	HeI	1s.14d - 1s.6f
				{4.0209	HI	14 - 6 (Hu14)
				{4.0234	HeI	1s.14p - 1s.6d
				{4.0377	HeI	1s.5f - 1s.4d
		4.039	s	{4.0409	HeI	1s.5f - 1s.4d
				{4.0490	HeI	1s.5g - 1s.4f
				{4.0506	HeII	10 - 8
				{4.0523	HI	5 - 4 (Br-α)
				{4.0545	HeI	1s.5d - 1s.4f
		4.066		4.0563	HeI	1s.5d - 1s.4f
						Band ends at 4.06 μm
SWS-Band 2A						Band starts at 4.05 μm
		4.031	}s	see above		
4.047	s	4.049	}s	see above		
4.120	w	4.123	w	4.1227	HeI	1s.5d - 1s.4p
				{4.1634	HeI	1s.13p - 1s.6d
4.166	w	4.168	w	{4.1689	HeI	1s.13d - 1s.6f
				{4.1694	HeI	1s.13d - 1s.6f
				{4.1708	HI	13 - 6 (Hu13)
4.219	w	4.218	w	4.2184	HeII	12 - 9
		4.241	w	4.2441	HeI	1s.5p - 1s.4d

Table A2. (continued)

AOT-1/s3		AOT-6		identification		
$\lambda_{\rm obs}$ (μm)				$\lambda_{\rm calc}$ (μm)	ion	configuration
		4.291	}s			
4.295	}s	4.296	}s	{4.2954	HeI	1s.3p - 1s.3s
	}		}	{4.2959	HeI	1s.3p - 1s.3s
	}		}	{4.2960	HeI	1s.3p - 1s.3s
4.315	}w	4.313	}w			
		4.337	w			
				{4.3678	HeI	1s.12p - 1s.6d
4.372	w			{4.3746	HeI	1s.12d - 1s.6f
				{4.3749	HeI	1s.12d - 1s.6f
		4.376	w	{4.3765	HI	12 - 6 (Hu12)
				{4.3859	HeI	1s.12p - 1s.6d
4.402	}w					
4.408	}w	4.406	w	4.4073	HeI	1s.7d - 1s.5p
				{4.6425	HeI	1s.7f - 1s.5d
				{4.6449	HeI	1s.7f - 1s.5d
4.651	}w	4.650	}s	{4.6506	HeI	1s.7g - 1s.5f
	}		}	{4.6516	HeI	1s.7h - 1s.5g
	}		}	{4.6521	HeI	1s.7f - 1s.5g
	}		}	{4.6533	HeI	1s.7d - 1s.5f
	}		}	{4.6538	HI	7 - 5 (Pf-β)
	}		}	{4.6543	HeI	1s.7d - 1s.5f
	}		}	{4.6617	HeI	1s.11p - 1s.6d
	}		}	{4.6637	HeI	1s.11f - 1s.6d
4.667	}		}	{4.6652	HeI	1s.11f - 1s.6d
		4.668	}	{4.6695	HeI	1s.11f - 1s.6g
			}	{4.6707	HeI	1s.11d - 1s.6f
			}	{4.6710	HeI	1s.11d - 1s.6f
		4.676	}w	{4.6725	HI	11 - 6 (Hu-ϵ)
4.696	w			{4.6950	HeI	1s.5s - 1s.4p
		4.699	w	{4.7000	HeI	1s.7d - 1s.5p
		4.757	}			
4.765		4.765	}	4.7635	HeII	8 - 7
				{5.1141	HeI	1s.10p - 1s.6d
				{5.1187	HeI	1s.10f - 1s.6d
				{5.1205	HeI	1s.10f - 1s.6d
		5.121	}	{5.1212	HeI	1s.10s - 1s.6p
			}	{5.1256	HeI	1s.10f - 1s.6g
			}	{5.1257	HeI	1s.10f - 1s.6g
			}	{5.1268	HeI	1s.10d - 1s.6f
			}	{5.1268	HeI	1s.15p - 1s.7s
		5.127	}	{5.1274	HeI	1s.10d - 1s.6f
5.129			}	{5.1287	HI	10 - 6 (Hu-δ)
		5.131	}			
						Band ends at 5.31 μm
SWS-Band 2B						Band starts at 5.30 μm
		5.525	w	5.5251	HI	16 - 7
5.578	w	5.578	}w	{5.5806	HeII	13 - 10
		5.591	}w	{5.5828	HeII	11 - 9
		5.887	}	{5.8861	HeI	1s.9p - 1s.6d
		5.897	}	{5.8964	HeI	1s.9f - 1s.6d
		5.897	}	{5.8989	HeI	1s.9f - 1s.6d
5.903		5.904	}	{5.9056	HeI	1s.9f - 1s.6g
			}	{5.9057	HeI	1s.9f - 1s.6g
			}	{5.9071	HeI	1s.9d - 1s.6f
			}	{5.9076	HeI	1s.9d - 1s.6f
		5.909	}	{5.9082	HI	9 - 6 (Hu-γ)
		5.914	}			
		5.922	}			

Table A2. (continued)

AOT-1/s3		AOT-6		identification		
λ_{obs} (μm)				λ_{calc} (μm)	ion	configuration
		5.947	}w	{5.9463	HeI	1s.14p - 1s.7d
			}	{5.9515	HeI	1s.9d - 1s.6p
			}	{5.9544	HeI	1s.14d - 1s.7f
			}	{5.9545	HeI	1s.14d - 1s.7f
		5.960	}w	{5.9568	HI	14 - 7
			}	{5.9670	HeI	1s.14p - 1s.7d
			}	{5.9692	HeI	1s.9p - 1s.6d
		5.972	}w			
		6.282	}w	{6.2794	HeI	1s.13p - 1s.7d
		6.285	}w	{		
		6.289	}w	{6.2895	HeI	1s.13d - 1s.7f
6.290		6.291	}w	{6.2906	HeI	1s.13d - 1s.7f
				{6.2919	HI	13 - 7
6.767	}	6.767	}	{		
	}		}	{6.7697	HeI	1s.12d - 1s.7f
	}		}	{6.7704	HeI	1s.12d - 1s.7f
	}	6.774	}	{6.7720	HI	12 - 7
	}					
	}			{6.8007	HeI	1s.12p - 1s.7d
6.809	}w			{6.8068	HeI	1s.12d - 1s.7p
		6.934	}			
6.944		6.944	}	6.9480	HeII	9 - 8
						Band ends at 7.01 μm
SWS-Band 2C						Band starts at 7.00 μm
		7.419	}			
		7.424	}			
		7.433	}	{7.4334	HeI	1s.6f - 1s.5d
		7.437	}	{7.4375	HeI	1s.3p - 1s.3s
			}	{7.4397	HeI	1s.6f - 1s.5d
7.454	}s	7.451	}s	{7.4538	HeI	1s.6g - 1s.5f
	}	7.456	}	{7.4561	HeI	1s.6h - 1s.5g
	}		}	{7.4562	HeI	1s.6h - 1s.5g
	}		}	{7.4568	HeII	12 - 10
	}		}	{7.4582	HeI	1s.6f - 1s.5g
	}		}	{7.4592	HeI	1s.8p - 1s.6d
	}	7.460	}s	{7.4599	HI	6 - 5 (Pf-α)
	}	7.465	}s	{7.4647	HeI	1s.6d - 1s.5f
	}			{7.4685	HeI	1s.6d - 1s.5f
	}					
	}			{7.4850	HeI	1s.8f - 1s.6d
	}	7.489	}s	{7.4889	HeI	1s.8f - 1s.6d
	}	7.496	}s	{7.4951	HI	17 - 8
7.498	}s		}	{7.4975	HeI	1s.8g - 1s.6f
			}	{7.4990	HeI	1s.8h - 1s.6g
			}	{7.4993	HeI	1s.8i - 1s.6h
			}	{7.4995	HeI	1s.8g - 1s.6h
			}	{7.4999	HeI	1s.8f - 1s.6g
			}	{7.5022	HeI	1s.8d - 1s.6f
			}	{7.5025	HI	8 - 6 (Hu-β)
		7.505	}s	{7.5039	HeI	1s.8d - 1s.6f
		7.510	}s	{7.5081	HI	11 - 7
		7.519	}			
		7.772	w	7.7804	HI	16 - 8
8.158	w			8.1549	HI	15 - 8
8.393	}w	8.397	}w	{8.404	[NiIV]	3d6.(3G).4s - 3d6.(3D).4s
	}		}	{8.405	[NiIV]	3d7 - 3d7
	}	8.410	}w			
8.415	}w	8.420	}w			
		8.432	}w			
		8.668	w	8.6645	HI	14 - 8

Table A2. (continued)

AOT-1/s3		AOT-6		identification		
λ_{obs} (μm)				λ_{calc} (μm)	ion	configuration
				{8.741	HeI	1s.10f - 1s.7d
		8.742	}	{8.745	HeI	1s.10f - 1s.7d
8.755		8.751	}	{8.754	HeI	1s.10f - 1s.7g
			}	{8.7582	HeI	1s.10d - 1s.7f
			}	{8.7599	HeI	1s.10d - 1s.7f
		8.761	}	{8.7601	HI	10 - 7
		8.952	w			
8.978	}w	8.980	}w	{		
	}		}	{8.99	[NeV]	2s2.2p2 - 2s2.2p2
8.997	}	9.007	}w	{8.993	[ArIII]	3s2.3p4 - 3s2.3p4
9.094	}w					
9.111	}w					
				9.3920	HI	13 - 8
9.705	}w			{9.7068	HeII	13 - 11
9.723	}w	9.713	w	{9.7135	HeII	10 - 9
10.056	w					
10.088	w					
		10.492	}s			
10.499	}s	10.498	}s			
	}		}	{10.5014	HeI	1s.12d - 1s.8f
	}		}	{10.5028	HeI	1s.12d - 1s.8f
	}		}	{10.5035	HI	12 - 8
	}	10.511	}s	{10.5104	[SIV]	3s2.(1S).3p - 3s2.(1S).3p
10.521	}s	10.522	}s			
10.637	w					
10.871	}	10.863	}			
	}		}	10.8821	HeI	1s.4p - 1s.4s
10.901	}	10.889	}			
10.942	w					
11.121	w					
		11.285	}	{11.2822	HeI	1s.9f - 1s.7d
			}	{11.288	HeI	1s.9f - 1s.7d
11.302		11.301	}	{11.3038	HeI	1s.9f - 1s.7g
			}	{11.304	HeI	1s.9f - 1s.7g
			}	{11.3087	HI	9 - 7
		11.311	}	{11.3107	HeI	1s.9d - 1s.7f
			}	{11.3125	HeI	1s.9d - 1s.7f
		11.320	}			
		11.330	}			
11.872	w					
11.938	}w					
11.957	}w					
12.152	}					
12.165	}					
12.372	s	see below				Band ends at 12.6 μm
SWS-Band 3A						Band starts at 12.3 μm
		12.248	}w			
		12.269	}w			
		12.289	}			
		12.306	}			
		12.318	}s	{12.3289	HeI	1s.7f - 1s.6d
		12.334	}s	{12.3379	HeI	1s.11p - 1s.8d

Table A2. (continued)

AOT-1/s3		AOT-6		identification		
λ_{obs} (μm)				λ_{calc} (μm)	ion	configuration
			}	{12.3394	HeI	1s.7f - 1s.6d
			}	{12.357	HeI	1s.11f - 1s.8d
12.361	s	12.353	}s	{12.3618	HeI	1s.7g - 1s.6f
		12.361	}s	{12.362	HeI	1s.11f - 1s.8d
			}	{12.3657	HeI	1s.7h - 1s.6g
			}	{12.3665	HeI	1s.7i - 1s.6h
			}	{12.3674	HeI	1s.7g - 1s.6h
			}	{12.3693	HeI	1s.7f - 1s.6g
			}	{12.3719	HI	7 - 6 (Hu-α)
			}	{12.375	HeI	1s.11f - 1s.8g
		12.379	}s	{12.3809	HeI	1s.7d - 1s.6f
			}	{12.3864	HeI	1s.11d - 1s.8f
			}	{12.3872	HI	11 - 8
			}	{12.3878	HeI	1s.7d - 1s.6f
			}	{12.3884	HeI	1s.11d - 1s.8f
		12.430	}w			
		12.575	}w	{12.5751	HeI	1s.7d - 1s.6p
			}	{12.585	HeI	1s.14d - 1s.9f
			}	{12.5853	HeI	1s.14d - 1s.9f
			}	{12.5871	HI	14 - 9
		12.604	}w			
				13.0336	HeI	1s.7p - 1s.6d
		13.116	}w			
13.127	w	13.128	}w	13.1283	HeII	11 - 10
		13.130	}w	13.129	[SV]	3s.3p - 3s.3p
		13.150	w			
		14.089	}w			
			}	{14.1345	HeI	1s.13p - 1s.9d
		14.160	}w	{		
			}	{14.1822	HeI	1s.13d - 1s.9f
			}	{14.1831	HI	13 - 9
		14.194	}w	{14.187	HeI	1s.13d - 1s.9f
15.059	}w					
15.099	}w					
15.147	}w					
15.175	}w					
15.530	}s	15.529	}s			
	}	15.542	}s			
15.556	}s	15.562	}s	15.554	[NeIII]	2s2.2p4 - 2s2.2p4
	}	15.575	}s			
15.626	}					
		16.167	}	{16.165	HeI	1s.10f - 1s.8d
			}	{16.173	HeI	1s.10f - 1s.8d
		16.186	}	{16.195	HeI	1s.10f - 1s.8g
16.202	w	16.205	}	{16.209	HI	10 - 8
		16.220	}	{16.2104	HeI	1s.10d - 1s.8f
		16.236	}	{16.2163	HeI	1s.10d - 1s.8f
						Band ends at 16.6 μm
SWS-Band 3C						Band starts at 16.5 μm
16.858	w	16.860	w	{16.8806	HI	12 - 9
				{16.8831	HeI	1s.12d - 1s.9f
				{16.886	HeI	1s.12d - 1s.9f
		17.171	vw			
		17.212	}w			
		17.227	}w	17.2228	HeI	1s.10s - 1s.8p
		17.262	w	17.2609	HeII	12 - 11
		17.288	w	17.2797	HeI	1s.10s - 1s.8p

Table A2. (continued)

AOT-1/s3		AOT-6		identification		
λ_{obs} (μm)				λ_{calc} (μm)	ion	configuration
		19.014	}w	{19.0131	HeI	1s.8f - 1s.7d
		19.039	}s	{		
19.030	}		}	{19.0464	HeI	1s.8g - 1s.7f
	}		}	{19.0465	HeI	1s.8g - 1s.7f
	}		}	{19.0523	HeI	1s.8h - 1s.7g
	}		}	{19.0536	HeI	1s.8i - 1s.7h
	}		}	{19.0539	HeI	1s.8k - 1s.7i
	}		}	{19.0544	HeI	1s.8h - 1s.7i
	}		}	{19.0551	HeI	1s.8g - 1s.7h
	}		}	{19.0581	HeI	1s.8f - 1s.7g
	}	19.063	}s	{19.0619	HI	8 - 7
	}	19.076	}s	{19.0769	HeI	1s.8d - 1s.7f
19.086	}			{19.0881	HeI	1s.8d - 1s.7f
19.115	}					
						Band ends at 19.6 μm
SWS-Band 3D						Band starts at 19.5 μm
22.336	w	22.331	w	22.3405	HI	11 - 9

Notes:
s = strong; w = weak; vw = very weak;
} = blend; and {= within emission feature.

References

Anderson L.S., 1989, ApJ 339, 558
Antokhin I., Betrand J.-F., Lamontagne R., Moffat A.F.J., Matthews J., 1995, AJ 109, 817
Barlow M.J., Roche P., Aitken D.A., 1988, MNRAS 232, 821 (B88)
Butler K., Zeippen C.J., 1994, A&AS 108, 1
Cardelli J.A., Clayton G.C., Mathis J.S., 1989, ApJ 345, 245
Churchwell E., Beiging J.H., van der Hucht, et al., 1992, ApJ 393, 329 (C92)
Cohen M., 1993, AJ 105, 1860
Conti P.S., Massey P., Vreux J.-M., 1990, ApJ 354, 359
Contreras M.E., Rodríguez L.F., 1999, ApJ 515, 762
Crowther P.A., 1997, In: Bedding T.R., Booth A.J., Davis J. (eds.) Fundamental Stellar Properties: The Interaction Between Observation and Theory. Proc. IAU Symp. 189, Kluwer, Dordrecht, 137
Crowther P.A., Smith L.J., 1997, A&A 320, 500
Crowther P.A., Smith L.J., Hillier D.J., Schmutz W., 1995a, A&A 293, 427
Crowther P.A., Hillier D.J., Smith L.J., 1995b, A&A 293, 407
de Graauw T., Haser L.N., Beintema D.A., et al., 1996, A&A 315, 49
Eenens P.R.J., Williams P.M., 1994, MNRAS 269, 1082
Hamann W.-R., Koesterke L., 1998a, A&A 335, 1003
Hamann W.-R., Koesterke L., 1998b, A&A 333, 251
Hamann W.-R., Koesterke L., Wessolowski U., 1995, A&A 299, 151
Herald J.E., Schulte-Ladbeck R.E., Hillier, J.D., 1999, In: van der Hucht K.A., Koenigsberger G., Eenens P.R.J. (eds.) Wolf-Rayet Phenomena in Massive Stars and Starburst Galaxies. Proc. IAU Symp. No. 193, ASP, San Francisco, 242
Hillier D.J., 1987, ApJS 63, 947
Hillier D.J., 1990, A&A 231, 111
Hillier D.J., 1991, A&A 247, 455

Hillier D.J., 1995, 163
Hillier D.J., Miller D.L., 1998, ApJ 496, 407
Hillier D.J., Miller D.L., 1999, ApJ 519, 354
Howarth I.D., 1983, MNRAS 203, 301
Lamers H.J.G.L.M., Najarro F., Kudritzki R.P., et al., 1996, A&A 315, 299
Lamontagne R., Moffat A.F.J., 1987, AJ 94, 1008
Langer N., Hamann W.-R., Lennon M., et al., 1994, A&A 290, 819
Leitherer C., Chapman J.M., Koriblaski B., 1997, ApJ 481, 898
Lépine S., Moffat A.F.J., 1999, ApJ 514, 909
Lundstrom I., Stenholm B., 1989, A&A 218, 199
Maeder A., 1991, A&A 242, 93
Maeder A., 1996, In: Vreux J.M., et al. (eds.) Wolf-Rayet Stars in the Framework of Stellar Evolution. Proc. 33rd Liège Int. Astroph. Colloq., Université de Liège, 39
Maeder A., 1999, In: van der Hucht K.A., Koenigsberger G., Eenens P.R.J. (eds.) Wolf-Rayet Phenomena in Massive Stars and Starburst Galaxies. Proc. IAU Symp. No. 193, ASP, San Francisco, 177
Marchenko S.V., Antokhin I.I., Betrand J.-F., et al., 1994, AJ 108, 678
Marchenko S.V., Moffat A.F.J., Eversberg T., et al., 1998, MNRAS 294, 642
Massey P., 1984, ApJ 281, 789
Meynet G., 1999, In: van der Hucht K.A., Koenigsberger G., Eenens P.R.J. (eds.) Wolf-Rayet Phenomena in Massive Stars and Starburst Galaxies. Proc. IAU Symp. No. 193, ASP, San Francisco, 218
Miller G.J., Chu Y.-H., 1993, ApJS 85, 137
Moffat A.F.J., 1996, In: Vreux J.M., et al. (eds.) Wolf-Rayet Stars in the Framework of Stellar Evolution. Proc. 33rd Liège Int. Astroph. Colloq., Université de Liège, 199
Moffat A.F.J., 1999, In: van der Hucht K.A., Koenigsberger G., Eenens P.R.J. (eds.) Wolf-Rayet Phenomena in Massive Stars and Starburst Galaxies. Proc. IAU Symp. No. 193, ASP, San Francisco, 278
Moffat A.F.J., Robert C., 1994, ApJ 421, 310
Moffat A.F.J., Drissen L., Lamontagne R., Robert C., 1988, ApJ 334, 1038
Moffat A.F.J., Drissen L., Robert C., 1989, In: Davidson K., Moffat A.F.J., Lamers H.J.G.L.M. (eds.) Physics of Luminous Blue Variables. Proc. IAU Coll. 113 Kluwer, Dordrecht, Ap&SSLib 157, 229
Moran J.P., Davis R.J., Spencer R.E., Bode M.F., Taylor A.R., 1989, Nat 340, 449
Morris P.W., van der Hucht K.A., Williams P.M., 1998, Ap&SS 255, 157
Morris P.W., van der Hucht K.A., Willis A.J., et al., 1999, In: van der Hucht K.A., Koenigsberger G., Eenens P.R.J. (eds.) Wolf-Rayet Phenomena in Massive Stars and Starburst Galaxies. Proc. IAU Symp. No. 193, ASP, San Francisco, 77
Najarro F., Hillier D.J., Kudritzki R.P., et al., 1994, A&A 285, 573
Najarro F., Krabbe A., Genzel R., et al., 1997, A&A 325, 700
Najarro F., Kudritzki R.P., Hillier D.J., et al., 1998a, In: Heras A.M., et al. (eds.) First *ISO* Workshop on Analytical Spectroscopy. ESA SP-419 ESA Pub. Div., Noordwijk, 167
Najarro F., Kudritzki R.P., Hillier D.J., et al., 1998b, In: Howarth I. (ed.) Boulder-Munich II: Properties of Hot, Luminous Stars. Proc. ASP Conf. Ser. 131, ASP, San Francisco, 57
Naqvi A.M., 1951, Thesis, Harvard
Niemela V.S., Shara M.M., Wallace D.J., Zurek D.R., Moffat A.F.J., 1998, AJ 115, 2047
Nugis T., Crowther P.A., Willis A.J., 1998, A&A 333, 956
Oke J.B., 1990, AJ 99, 1621
Pelan J., Berrington K.A., 1995, A&AS 110, 209
Rieke G.H., Lebofsky M.J., 1985, ApJ 288, 618
Robert C., Moffat A.F.J., Bastein P., Drissen L., St.-Louis N., 1989, ApJ 347, 1034
Saraph H.E., Storey P.J., 1999, A&AS 134, 369
Schutte W.A., van der Hucht K.A., Whittet D.C.B., et al., 1998, A&A 337, 261
Skinner S.L., Itah M., Nagase F., Zhekov S.A., 1999, ApJ 524, 394
Smith J.D., Houck, J.R., 1999, In: van der Hucht K.A., Koenigsberger G., Eenens P.R.J. (eds.) Wolf-Rayet Phenomena in Massive Stars and Starburst Galaxies. Proc. IAU Symp. No. 193, ASP, San Francisco, 107
Smith L.F., 1968, MNRAS 138, 109
Smith L.F., Shara M.M., Moffat, A.F.J., 1996, MNRAS 281, 163
Steenman H., Thé P.S.. 1989, Ap&SS 159, 189
Stickland D.J., Lloyd C., Willis A.J., 1985, A&A 150, 9
van der Hucht K.A., Hidayat B., Admiranto A.G., Supelli K.R., Doom C., 1988, A&A 199, 217
van der Hucht K.A., Williams P.M., Spoelstra T.A.Th., Swaanenvelt J.P., 1995, In: van der Hucht K.A., Williams P:M. (eds.) Wolf-Rayet stars: binaries; colliding winds; evolution. Proc. IAU Symp. No. 163, Kluwer, Dordrecht, 559
van der Hucht K.A., Morris P.W., Williams P.M., et al., 1996, A&A 315, 193
Watson S.K., Davis R.J., Williams P.M., 1999, In: van der Hucht K.A., Koenigsberger G., Eenens P.R.J. (eds.) Wolf-Rayet Phenomena in Massive Stars and Starburst Galaxies. Proc. IAU Symp. No. 193, ASP, San Francisco, 396
Williams P.M., van der Hucht K.A., Thé P.S., 1987, A&A 182, 91
Williams P.M., Dougherty S.M., Davis R.J., et al., 1997, MNRAS 289, 10 (W97)
Willis A.J., 1991, In: van der Hucht K.A., Hidayat B. (eds.) Wolf-Rayet Stars and Interrelations with Other Massive Stars in Galaxies. Proc. IAU Symp. No. 143, Kluwer, Dordrecht, 265
Wright A.E., Barlow M.J., 1975, MNRAS 170, 41